INTERNATIONAL JOURNAL OF CLIMATOLOGY
Int. J. Climatol. (2017)
Published online in Wiley Online Library
(wileyonlinelibrary.com) DOI: 10.1002/joc.5132

RMetS
Royal Meteorological Society

Space-time variability of extreme rainfall in the River Nile basin

Charles Onyutha[a,b]* and Patrick Willems[a]
[a] *Hydraulics Laboratory, KU Leuven, Leuven, Belgium*
[b] *Faculty of Technoscience, Muni University, Arua, Uganda*

ABSTRACT: In this study, spatio-temporal variability in daily rainfall extremes based on $0.5^\circ \times 0.5^\circ$ gridded data over the Nile basin was analysed using the quantile perturbation method. The co-occurrence of the extreme rainfall variability with the variation in the large-scale ocean–atmosphere conditions was also investigated. Based on a 15-year moving window, it was found that the extreme rainfall shows oscillatory behaviour over multi-decadal time scales. The latitudinal difference in the multi-decadal extreme rainfall oscillations divides the study area into the Northern, Central, and Southern regions. The variability in the extreme rainfall of the Central region is dominantly driven by the variation in the sea surface temperatures of the Atlantic and Pacific Oceans. For the Southern region, extreme rainfall variability is linked to the anomalies in the sea level pressure of the North Atlantic Ocean and the variation in the sea surface temperature of the Indian Ocean. The variation in the extreme rainfall of the Northern region corresponds to the anomalies in sea surface temperatures of the Indian and Atlantic Oceans as well as from the Pacific Ocean.

KEY WORDS climate variability; climate indices; rainfall variability; River Nile basin; quantile perturbation method; rainfall extremes

Received 11 August 2016; Revised 9 April 2017; Accepted 18 April 2017

1. Introduction

Disasters (e.g. landslides, floods, drought, etc.) that are related to the scarcity or surplus of water are directly based on the occurrences of extreme rainfall events, which in turn tend to be influenced by climate variability. Eventually, there is a need to comprehend the variation in historical or observed hydro-meteorological variables and associated drivers (Onyutha, 2016a; Pradhan *et al.*, 2017; Zilli *et al.*, 2017).

The Nile basin is not exceptional to the occurrences of the rainfall-based disasters. Heavy rainfall events seem common in Ethiopia as well as the equatorial region. Some of the recent disasters that claimed lives and property in the study area include: (1) the devastating flooding in the Kasese district of Uganda in the early May 2013 and mid-May 2016, and (2) the disastrous floods and landslides in Oromia and the Southern Nations, Nationalities and People's Region of Ethiopia in May 2016. For regional planning, operation and management of risk-based water resources applications in the Nile basin, understanding the variability of extreme rainfall is essential. High rainfall intensities cause floods, whereas drought conditions are of importance for agricultural applications. It turns out to be unfortunate that for the case of the River Nile basin, the analyses of rainfall variability are confined to sub-basins (Taye and Willems, 2012; Nyeko-Ogiramoi *et al.*, 2013; Berhane *et al.*, 2014), sub-regions (Phillips and McIntyre, 2000; Onyutha, 2016b), or only rainfall totals but no extremes are considered (Block and Rajagopalan, 2007; Abtew *et al.*, 2009; Berhane *et al.*, 2014; Onyutha and Willems, 2015). Clarity in the spatio-temporal rainfall variability in the Nile basin is also often affected by the poor distribution of meteorological stations. Even worse, the data have short-term record length and are of questionable quality.

Therefore, the aim of this study is to investigate the variability in extreme rainfall using high-resolution ($0.5^\circ \times 0.5^\circ$) gridded long-term daily rainfall which spatially covers the entire region where the Nile basin is located. The spatio-temporal differences in the linkages of the rainfall variability across the study area to large-scale ocean–atmosphere interactions are also assessed.

2. Materials and methods

2.1. Study area

The River Nile has a catchment area of about $3\,400\,000\,km^2$ (Figure 1). As the world's longest river under arid condition, the River Nile has 11 riparian countries including Burundi, Rwanda, Uganda, Kenya, Tanzania, South Sudan, Democratic Republic of Congo, Sudan, Eritrea, Ethiopia, and Egypt. The rainfall over the Nile basin is highly contrasted with some parts experiencing hyper-arid conditions, while other areas are sub-humid. The Southernmost part of the basin shows

* Correspondence to: C. Onyutha, Hydraulics Laboratory, KU Leuven, Kasteelpark Arenberg 40, 3001 Leuven, Belgium. E-mail: conyutha@gmail.com

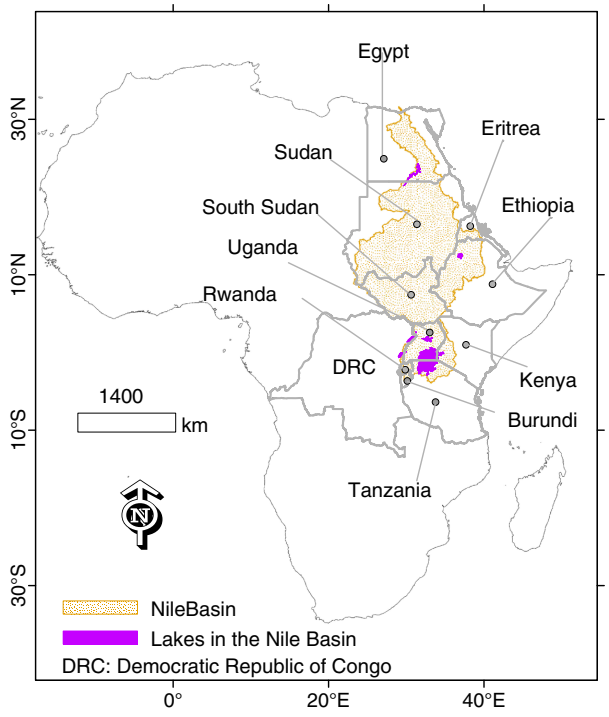

Figure 1. The Nile basin and the river riparian countries (Onyutha, 2016a). [Colour figure can be viewed at wileyonlinelibrary.com].

bimodal rainfall patterns (Nicholson, 1996) while the Central region has a unimodal rainy season. For the Northernmost part of the basin, which has arid conditions, the rainfall is of an unclear pattern, though somewhat rainy seasons tend to occur during the March to May, and October through December to February periods (Onyutha and Willems, 2015).

2.2. Rainfall data and climate indices

Global daily rainfall data of the Princeton global forcings (PGFs) (Sheffield *et al.*, 2006) were obtained in gridded ($0.5° \times 0.5°$) form from the link http://hydrology.princeton.edu/data/pgf/0.5deg/ (accessed 12 February 2016). The PGFs, which cover the period 1948–2010, are of the observational-reanalysis hybrid type (Sheffield *et al.*, 2006). More specifically, the PGF-based data are derived from a combination of the NCEP–NCAR reanalysis dataset (Kalnay *et al.*, 1996) with several other observational-based rainfall products including the TRMM, the CRU TS2.0, the GPCP, and the NASA Langley Research Center SRB products (Sheffield *et al.*, 2006). Compared to other freely available rainfall products, the PGF-based data are commonly used due to their robustness for variability analyses as demonstrated in a number of studies (Hoell *et al.*, 2015; Zeng and Cai, 2016; Onyutha and Willems, 2017).

Daily series for the Nile basin covering the region of latitudes from 31°N to 5°S in the north–south direction, and longitudes over the range 24–40°E in the west–east direction were extracted from the global PGF-based data. For variability analyses, various series of extreme rainfall were extracted from the daily data including: (1) the mean of ten highest rainfall intensities (HRI) in each year, (2) the percentage of dry days (PDD) in each year, and (3) the longest period of dry days or the maximum dry spell (MDS) in each year. In this study, a dry day was considered as that with rainfall intensity below 1 mm/day.

To investigate the linkage of extreme rainfall variability to large-scale ocean–atmosphere conditions, several climate indices were obtained including: the Indian Ocean dipole (IOD) index, Atlantic multidecadal oscillation (AMO) index (van Oldenborgh *et al.*, 2009), North Atlantic oscillation (NAO) index (Jones *et al.*, 1997), and Niño 3 index (Trenberth, 1997; Rayner *et al.*, 2003). The IOD index refers to the anomalous sea surface temperature difference between the western (50–70°E and 10°S to 10°N) and the South eastern (90–110°E and 10°S to 0°N) equatorial Indian Ocean. According to van Oldenborgh *et al.* (2009), the AMO index refers to the sea surface temperature averaged over 25–60°N, 7–70°W minus the regression on global mean temperature. The NAO index is defined as the normalized sea level pressure difference between SW Iceland (Reykjavik), Gibraltar, and Ponta Delgada (Azores). The Niño 3 index is defined as the area-averaged sea surface temperature anomaly over the region 150–90°W and 5°S to 5°N. The monthly climate indices and/or series were downloaded from the following websites or databases:

a. http://www.jamstec.go.jp/frcgc/research/d1/iod (accessed 20 January 2014) for IOD,
b. http://climexp.knmi.nl/data/iamo_hadsst2.dat (accessed 29 January 2013) for AMO,
c. http://www.esrl.noaa.gov/psd/gcos_wgsp/Timeseries/NAO/ (accessed 16 April 2016) for NAO, and
d. http://www.esrl.noaa.gov/psd/gcos_wgsp/Timeseries/Nino3/ (accessed 29 January 2013) for Niño3.

For variability analyses, the monthly series of the climate indices were converted to annual time scale as considered for the gridded rainfall.

2.3. Computation of rainfall variability

Variability was derived in terms of anomalies in extreme quantiles computed by the quantile perturbation method (QPM) (Willems, 2013). By considering quantiles, frequency, and amplitude of the extremes are combined in the anomaly computation. Because of its robustness, the QPM was applied in several studies on rainfall variability in the study area (Taye and Willems, 2012; Nyeko-Ogiramoi *et al.*, 2013; Onyutha and Willems, 2015). To apply the QPM, a block length is required to extract sub-series. In this study, 15-year block length was selected because of its suitability for analyses of rainfall variability in the study area (Onyutha and Willems, 2015). Several sub-series, each characterized by the stipulated block length, are extracted from the full time series in an overlapping way through continuous sliding of the time slice by one time unit of the series (i.e. 1 year in this case). The values from each sub-series are sorted from the highest to the lowest; where after the exceedance probability is computed for

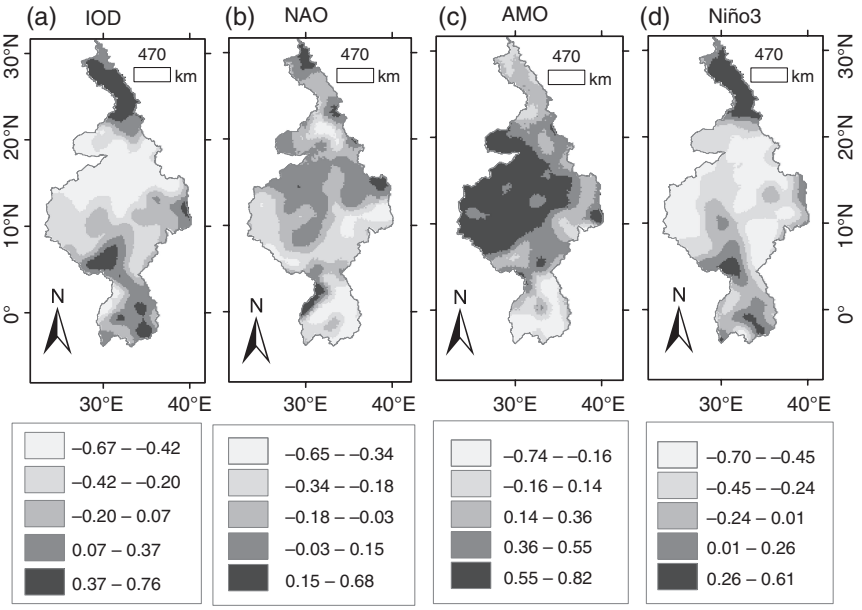

Figure 2. Correlation between QPM anomalies for the HRI and (a) IOD, (b) NAO, (c) AMO, and (d) Niño 3.

each of these values. The same procedure is repeated for the values in the full time series. In the next step, comparison is made of the values (quantiles) with the same exceedance probability in the sub-series and the full series to derive anomalies in terms of ratios of the quantiles based on the sub-series to those of the full time series. For each time slice, the perturbation factor is obtained as the average of all the anomalies above a stipulated exceedance probability.

Under the null hypothesis (H_0) that the variability is due to natural randomness, confidence interval bounds for verifying the H_0 are constructed by applying the nonparametric bootstrapping technique. The full time series is reshuffled 1000 times and the QPM is applied to each of the series with the new temporal sequence. Based on the 1000 anomaly values obtained, after sorting, upper and lower 95% confidence bounds are taken as the 25th and 975th anomaly values. If the QPM anomalies from the original series (i.e. the one not reshuffled) fall outside the confidence interval, the H_0 is rejected; otherwise, it is accepted.

The QPM was applied to derive anomalies for the HRI, PDD, and MDS series at each grid point. Anomalies were also computed for the climate indices. Temporal variability of extreme rainfall series (HRI, PDD, and MDS) along with climate indices were assessed using correlation analyses.

3. Results and discussion

3.1. Variability in the HRI

Figure 2 shows the spatial distribution of the correlation between variability in the extreme high rainfall and climate indices. It is noticeable that the HRI of the equatorial region (or the Southern part) of the basin is linked to the IOD (Figure 2(a)), NAO (Figure 2(b)), and AMO (Figure 2(c)). These results are consistent with the findings from previous studies (Tierney *et al.*, 2013; Onyutha and Willems, 2015) conducted for the areas including the equatorial region. Some evidence is also visible on the linkage of the HRI to Niño 3 (Figure 2(d)). Generally, there are also several studies which document the linkage of rainfall variability in the equatorial region to the El Niño Southern Oscillation (ENSO) (Nicholson and Kim, 1997; Phillips and McIntyre, 2000; Schreck and Semazzi, 2004; Onyutha and Willems, 2015).

The variation in HRI of the Central part of the study area is influenced by IOD, AMO, and Niño 3 (Figures 2(a), (c) and (d). Mainly positive (negative) correlation was obtained between HRI and AMO (IOD and Niño 3). The variability of the annual maximum rainfall events observed over the upper Blue Nile basin located in the Central part of the study area was found mostly linked to the changes in sea surface temperature or sea level pressure in the Pacific and Atlantic Oceans (Taye and Willems, 2012). Jury (2010) reported that the rainfall variability in the Southern part of Ethiopia is influenced by the cold phase of the Pacific Decadal Oscillation as well as by the Southern meridional overturning circulation, whereas in the Northern region it is enhanced by the warm phase of AMO. In Ethiopia, the Northern part is basically characterized by the tropical easterly jet and has a unimodal rainy season, whereas the rainfall in the Southern area exhibits a bimodal pattern (Jury, 2010). The rainfall variability for the Central part of the Nile basin was also evidenced to be linked to the ENSO (Seleshi and Demaree, 1995; Seleshi and Zanke, 2004; Abtew *et al.*, 2009; Jury, 2010; Diro *et al.*, 2011; Onyutha and Willems, 2015). For the Northern part of the basin, the possible drivers of the variability in rainfall extremes emanate from the Indian Ocean (Figure 2(a)) or Pacific Ocean (Figure 2(d)). Moreover, positive correlation generally exists between HRI and IOD, or HRI and Niño 3.

Based on the spatial correlation map shown in Figure 2, the River Nile basin can be divided into three regions, namely Southern (5°S to 5°N), Central (5–20°N), and Northern (20–30°N). These regions, which are consistent with those found in a recent study by Onyutha and Willems (2015), correspond to the spatially contrasting distribution of rainfall in response to the latitudinal migration of the Inter-Tropical Convergence Zone (ITCZ) across the study area. The ITCZ tends to stay longer in the Southern than Central part of the study area and never reaches the North of Sudan or Egypt, i.e. areas characterized by arid conditions. It is possible that the variation in extreme rainfall of the Northern region might be under the influence of the North African monsoon. However, the variation in the rainfall of the Southern region may be controlled by the changes in the equatorial circulation. Furthermore, the spatial distribution of the rainfall in the Southern region of the study area is also influenced by regional topographical features (Onyutha *et al.*, 2016). In the equatorial region, some of the regional features which may interactively modify the variation in rainfall include the water bodies (e.g. Lake Victoria, Lake Kyoga, Lake Albert, Lake Turkana) (Thiery *et al.*, 2015) and mountains (such as Mount Elgon, Mount Rwenzori, and Mount Kenya). For instance, Thiery *et al.* (2015) found that by inducing circular airflow with over-lake convective inhibition during daytime and the reversed pattern at night, the Lake Victoria has a profound influence on atmospheric dynamics and stability with respect to the East African regional climate. In the Central region of the study area, e.g. over Ethiopia, the distribution of rainfall is also controlled by the Ethiopian Highlands, which tend to receive complex pattern of rainfall following the blockage of the moist unstable westerly flow of the Congo Air from reaching the coastal areas of Central region of the study area (Nicholson, 1996).

Figure 3 shows the temporal variability of HRI along with climate indices. For the equatorial region (Figure 3(a)), the HRI oscillation highs (i.e. epochs of 'above-normal' extreme rainfall events) were from the late 1950s to mid-1960s, and again in the late 1990s. On the other hand, oscillation lows (i.e. epochs of 'below-normal' extreme rainfall events) were in the early 1950s and the 1980s. For the Central region (Figure 3(b)), the extreme high rainfall events were above the reference in the 1950s and early 1960s. The extreme rainfall was below the reference from the late 1960s to the 1980s. Generally, the period from the late 1960s to the 1980s has been sufficiently documented for the decrease in rainfall in the Central part of the study area (Hulme, 1992; Zhang *et al.*, 2012; Onyutha and Willems, 2015). For the annual rainfall, this decrease in rainfall was about 30% (Hulme, 1992). Furthermore, this rainfall decrease led to much shorter rainy seasons in the 1970s and the 1980s, mainly due to an earlier end. In the Northern part of the basin, the extreme rainfall events were below (above) their long-term average from the 1940s to the early 1980s (mid-1980s to the late 2000s) (Figure 3(c)). These results for all three regions are consistent with the findings from the spatio-temporal

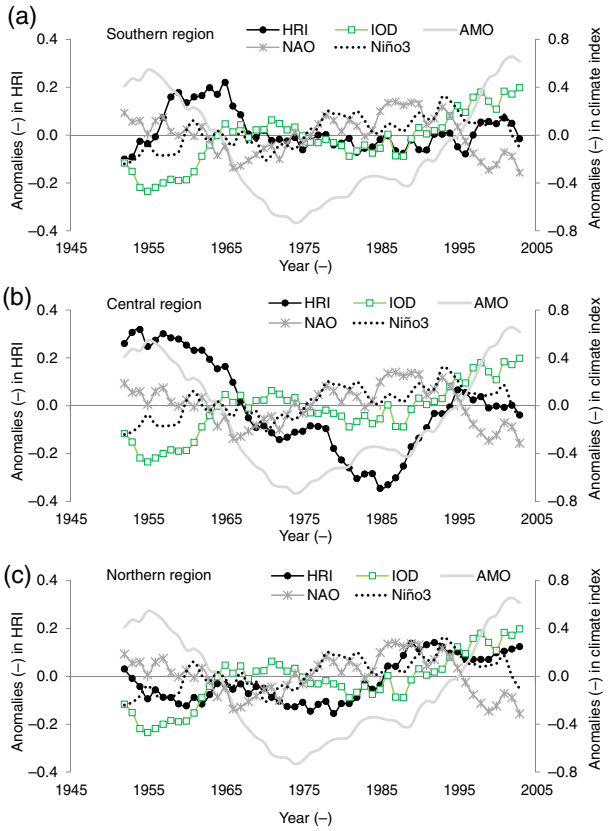

Figure 3. Variation in HRI along with climate indices. (a) Southern region, (b) Central region, and (c) Northern region. [Colour figure can be viewed at wileyonlinelibrary.com].

variability analysed in a previous study (Onyutha and Willems, 2015) based on observed annual rainfall totals.

To find out what percentage of variance in the rainfall extremes can be attributed to the selected climate indices, multiple linear regression equation (MLRE) was used. The statistical 'goodness-of-fit' metric coefficient of determination (R^2) was calculated for the various combinations of the climate indices as predictors. It is well-known that when more predictors are added to the MLRE, the value of R^2 gets higher. Therefore, to attach some punitive measure to the addition of many variables, an adjusted R^2 (Ezekiel, 1930) was adopted as summarized in Table 1. The adjusted R^2 was optimized through minimization of the mean squared error. When all the four climate indices were used as predictors in the MLRE, the adjusted R^2 obtained was 28.1, 67.0, and 70.3% for the Southern, Central, and Northern regions, respectively. However, when the climate indices were used individually as predictors, the highest value of the adjusted R^2 was obtained using NAO (12.7%), AMO (50.1%), and IOD (29.2%) for the Southern, Central, and Northern regions, respectively. For each region, the climate index with the highest adjusted R^2 was the best in describing the HRI variation. In other words, without considering the most suitable large-scale ocean–atmosphere condition, even if two or three climate indices were combined, the adjusted R^2 still remained low.

Table 1. Adjusted R^2 (%) in predicting HRI using climate indices.

Predictor	Region		
	Southern	Central	Northern
IOD (I)	0.40	12.7	29.2
AMO (A)	10.6	50.1	12.7
NAO (N)	12.7	2.90	0.30
Niño 3 (E)	1.50	20.8	14.1
I, A	10.8	59.6	44.8
I, N	20.7	29.6	44.0
I, E	1.50	24.9	32.7
A, N	19.7	50.2	14.2
A, E	11.0	60.9	33.0
N, E	12.9	21.2	14.2
I, A, E	11.0	65.0	51.5
I, N, E	23.3	31.9	44.1
A, N, E	19.7	61.0	33.0
I, A, N	25.2	65.4	70.3
I, A, N, E	28.1	67.0	70.3

Generally, the percentage of the HRI that can be attributable to the climate indices depends on the suitability of the oceanic areas from which the sea level pressure or sea surface temperature can resonate well with the variation in the extreme rainfall of the region under consideration. The influence of atmospheric circulation on rainfall distribution over several regions of the study area can be affected by the differences in the sea level pressure (SLP) from the various oceans. For the three regions of the study area, Onyutha and Willems (2015) already investigated the co-variation of rainfall for the Southern, Central, and Northern region of the study area with the sea level pressure difference between the Indian and Atlantic oceans, as well as the Indian and Pacific oceans. Onyutha and Willems (2015) showed that, for instance, the difference in the sea level pressure taken over the Pacific and Indian Oceans is not significantly (at 5% level) correlated with the anomalies in the annual rainfall of the Southern region. The insignificance of this correlation is because, according to Tierney *et al.* (2013), it is mainly the Indian Ocean sea surface temperature that drives East African rainfall variability by altering the local Walker circulation, whereas the influence of the Pacific Ocean is minimal. Instead, the variability in the annual rainfall of the Southern region was shown to be significantly (at 5% level) explained by the differences in sea level pressure from the North Atlantic and Indian Oceans (Onyutha and Willems, 2015). For the rainfall variability of the Central region of the study area, influences emanate from the Pacific and Indian Oceans. However, influences for the variability of rainfall in the Northern region come partially from the Indian, Atlantic, and Pacific oceans.

3.2. Variability in the lowest rainfall intensities

3.2.1. Percentage of dry days (PDD)

Figure 4 shows how the PDD variability is linked to the large-scale ocean–atmosphere conditions. The PDD of the Northern extreme end of the study area is negatively correlated with IOD and Niño 3 (Figures 4(a) and (d)). The PDD variability over the Southern region is positively correlated with AMO (Figure 4(c)). Over a large area of the Central part, the PDD variability is shown to be positively (negatively) correlated with the Niño 3 (AMO) (Figures 4 (c) and (d)). Generally, the influence of climate indices on the PDD variability (Figure 4) is not as spatially coherent as that for the HRI (Figure 2). This suggests that, apart from the influence from the large-scale ocean–atmosphere

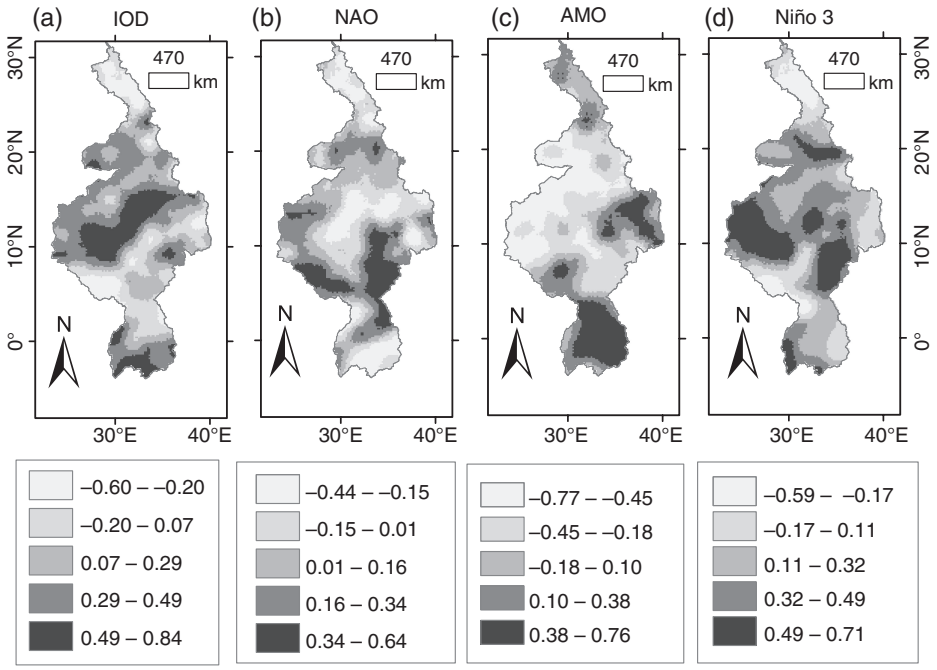

Figure 4. Correlation between QPM anomalies for the PDD in each year and (a) IOD, (b) NAO, (c) AMO, and (d) Niño 3.

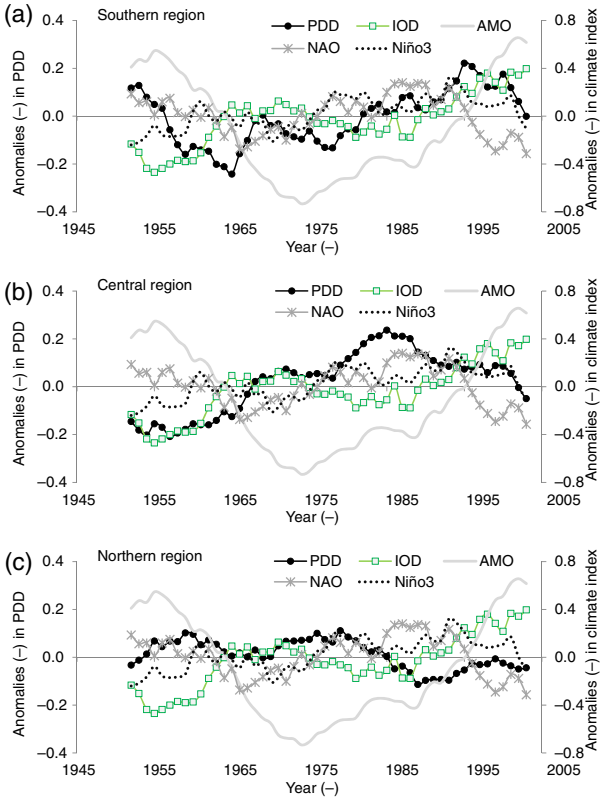

Figure 5. Temporal variation of PDD along with the climate indices. (a) Southern region, (b) Central region, and (c) Northern region. [Colour figure can be viewed at wileyonlinelibrary.com].

interactions on extreme low rainfall, the drought conditions over the various regions of the study area may also be due to other drivers. Such drivers may include the influence from topographical features, and spatial difference in the micro-climate. Using a physically based or detailed model, which can reasonably reproduce the hydro-climatic conditions across the study area, the influence of regional features such as water bodies and changes in land cover or use on the rainfall distribution may be investigated.

Figure 5 shows the temporal variability of the climate indices along with the averaged PDD over the considered regions. The PDD oscillation low (high) in the Southern region (Figure 5(a)) was from the mid-1950s to early 1970s (1980s to 2000s). For the Central region (Figure 5(b)), the PDD was above (below) the long-term mean from the late 1970s to early 2000s (1950s to mid-1960s). In the Northern part of the basin (Figure 5(c)), the PDD exhibited an oscillation low (high) from the early 1980s to the late 2000s (1950s and 1970s).

The statistical measure of the co-occurrence of the PDD and climate indices shown in (Figure 5) is summarized in Table 2. By combining all the four climate indices as predictors in the MLRE, the adjusted R^2 was 41.5, 68.6, and 57.8% for the Southern, Central, and Northern regions, respectively. When the climate indices were considered individually as the predictor, the highest value of the adjusted R^2 was obtained using the IOD (10.3%), Niño3 (35.3%), and IOD (21.5%) for the Southern, Central, and Northern regions, respectively.

Table 2. Adjusted R^2 (%) in predicting PDD using climate indices.

Predictor	Region		
	Southern	Central	Northern
IOD (I)	10.3	20.7	21.5
AMO (A)	9.90	33.3	3.60
NAO (N)	1.60	3.80	3.00
Niño 3 (E)	7.40	35.3	11.7
I, A	21.7	50.7	26.4
I, N	22.0	45.7	44.4
I, E	13.0	41.6	24.9
A, N	13.5	34.1	8.00
A, E	21.3	57.7	18.4
N, E	7.90	35.6	12.6
I, A, E	26.9	64.1	31.5
I, N, E	22.0	50.8	45.2
A, N, E	22.9	55.1	20.2
I, A, N	41.5	62.1	57.3
I, A, N, E	41.5	68.6	57.8

3.2.2. *Maximum dry spell (MDS)*

Figure 6 shows the strength of the linkage of the MDS anomalies to the climate indices. As seen from Figure 6(d), the MDS of the extreme Northern part is negatively correlated with IOD and Nino 3. For the western part of the equatorial region, MDS is positively correlated with AMO (Figure 6(c)). For the Central region, the correlation between MDS and climate indices (Figures 6(a)–(d)) is not as spatially coherent as that between HRI and the climate indices (Figures 2(a)–(d)). The variability in the drought conditions in the Central part of the basin, though partly explained by the anomalies in the climate indices, was found to be highly linked with the variability in the moisture flux (Long *et al.*, 2000; Zhang *et al.*, 2012). Recently, Zhang *et al.* (2012) found that drought conditions in this part of the Nile basin result from the tendency of the Northeasterly wind in Sudan, which limits Northward propagation of moisture flux to the Northern part of Sudan (and eventually Egypt). Based on the analysis of atmospheric water and moisture fluxes in West African Monsoon, the rainfall during the dry season in the Sahel region (which is located in the Central part of the basin) was found to be clearly dominated by the easterly anomalies in the moisture flux South of 15°N (Fontaine *et al.*, 2003).

The temporal variation in the MDS along with climate indices is shown in Figure 7. The MDS of the Northern part of the basin (Figure 7(c)) was above (below) the reference in the 1950s to 1970s (mid-1980s to around 2000). For the Central region (Figure 7(b)), the MDS exhibited oscillation lows (high) in the 1950s and 1990s (from the late 1960s to around 1990). For the equatorial region (Figure 7(a)), the MDS was below (above) the reference in the mid-1990s (from the mid-1960s to late 1970s).

The strength of the linkage of MDS variability to climate indices shown in (Figure 7) is summarized in Table 3. By combining all the four climate indices as predictors in the MLRE, the adjusted R^2 was 38.5, 73.9, and 80.5% for

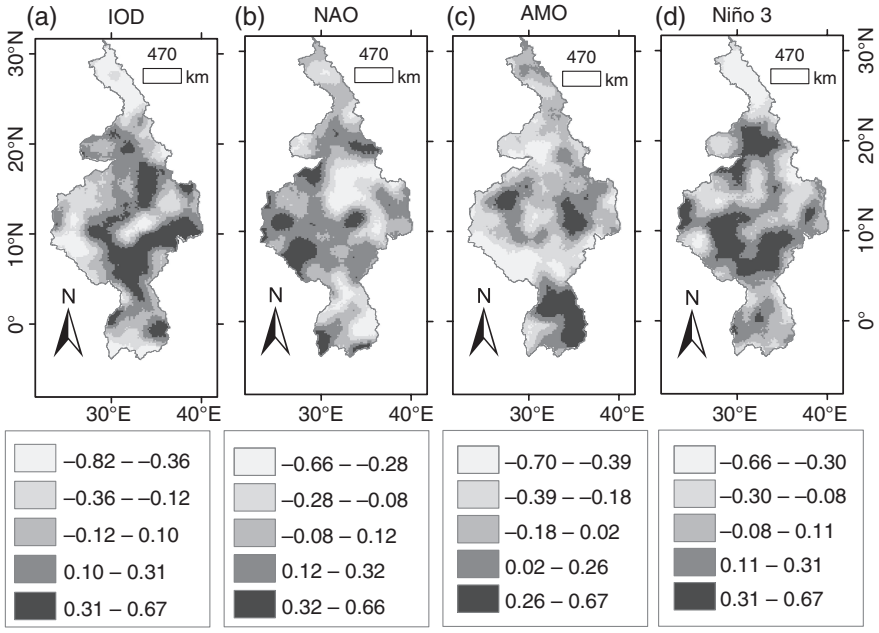

Figure 6. Correlation between QPM anomalies for the MDS in each year and (a) IOD, (b) NAO, (c) AMO, and (d) Niño 3.

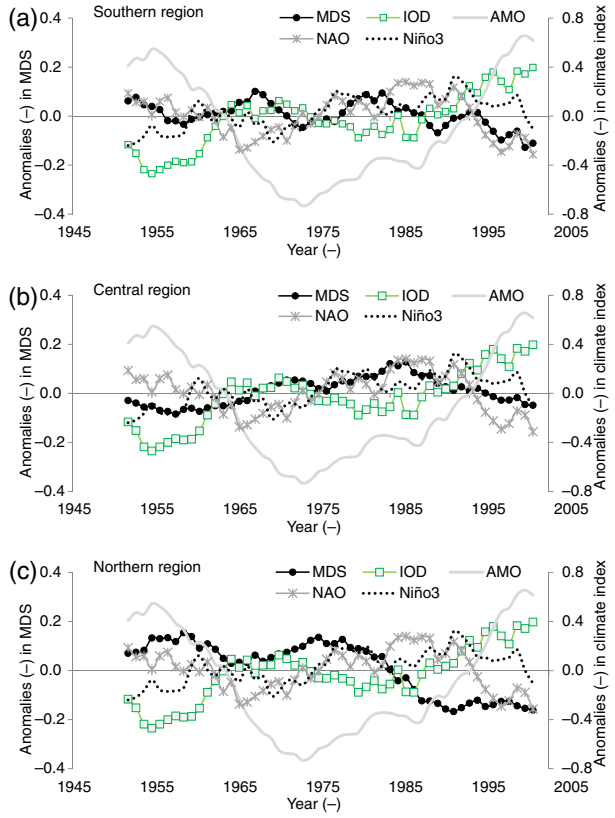

Figure 7. Temporal variation in the MDS along with climate indices. (a) Southern region, (b) Central region, and (c) Northern region. [Colour figure can be viewed at wileyonlinelibrary.com].

the Southern, Central, and Northern regions, respectively. When the climate indices were considered individually, the largest percentage of MDS variance was found to be explained by IOD (21.8%), AMO (54.7%), and IOD (52.0%) for the Southern, Central, and Northern regions, respectively.

Table 3. Adjusted R^2 (%) in predicting MDS using climate indices.

Predictor	Region		
	Southern	Central	Northern
IOD (I)	21.8	3.60	52.0
AMO (A)	12.8	54.7	6.00
NAO (N)	5.30	16.8	0.60
Niño 3 (E)	2.60	15.1	25.1
I, A	37.1	56.7	60.7
I, N	21.9	38.6	63.7
I, E	21.9	15.3	58.2
A, N	15.6	62.2	6.10
A, E	18.2	61.1	37.0
N, E	10.2	25.8	29.1
I, A, E	37.4	61.4	70.1
I, N, E	21.9	38.7	64.4
A, N, E	23.0	66.3	39.2
I, A, N	38.5	73.9	79.6
I, A, N, E	38.5	73.9	80.5

It is possible that the attribution of the variation in extreme rainfall metrics such as HRI, PDD, and MDS to the large-scale ocean–atmosphere conditions may be influenced by other factors. For instance, Onyutha and Willems (2017) recently showed that due to the increase in the heterogeneity of rainfall over the study area, as the size of the spatial domain for analysis increases, the climate indices explain rainfall variability more suitably at a regional than location-specific spatial scale. Furthermore, for a region that is not perfectly homogenous as the study area, the occurrences of extreme rainfall conditions can be influenced in a synergistic way by the variation of two or more possible drivers. For instance, the variation of extreme rainfall of a particular region can be linked to both of the ENSO episodes including the warm (El Niño) and

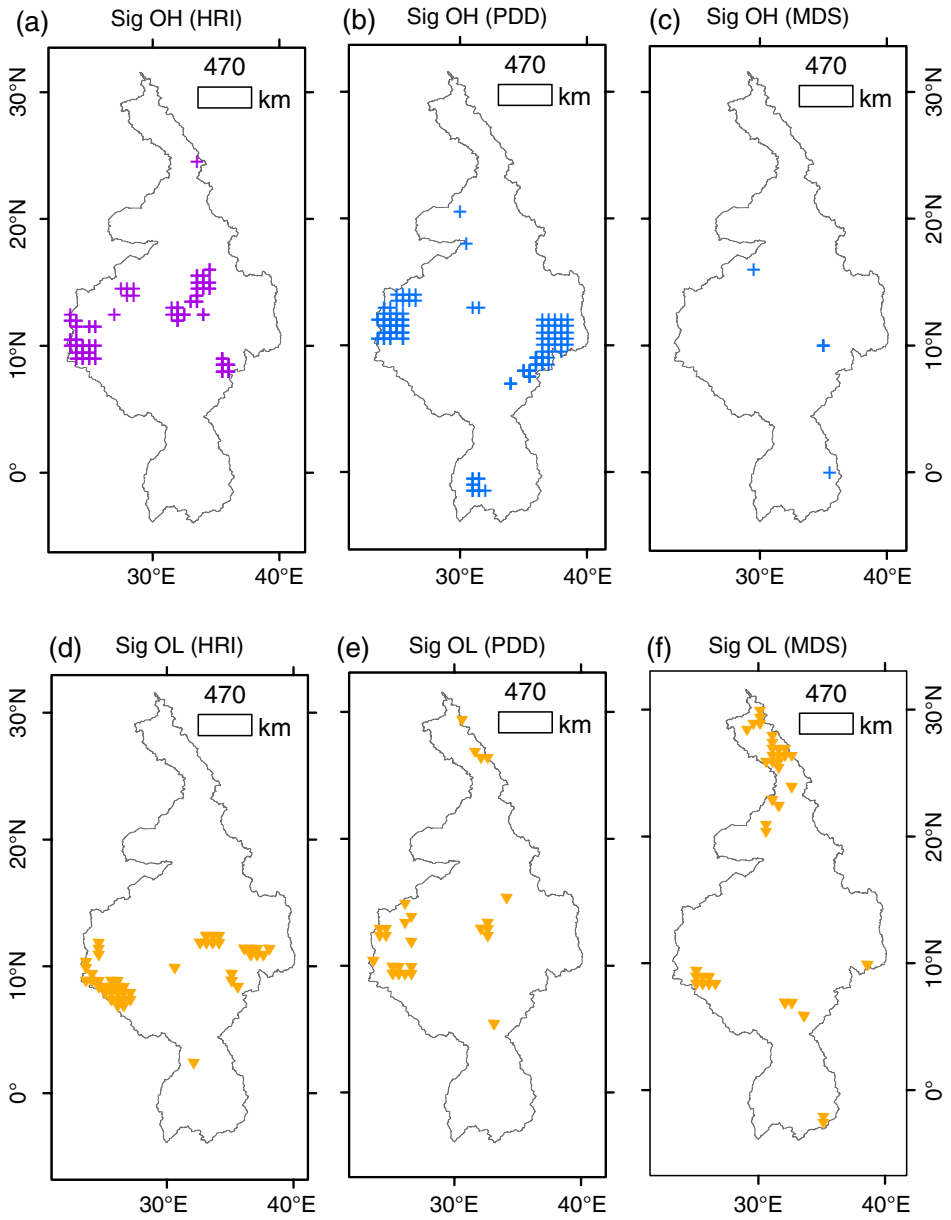

Figure 8. Locations with QPM anomaly significant (sig) at 5% level for the (a, d) HRI, (b, e) PDD, and (c, f) MDS. OH and OL denote positive and negative anomalies respectively. [Colour figure can be viewed at wileyonlinelibrary.com].

cold (La Niña) phases, which are known to bring about conditions that are respectively wetter and drier than the normal one.

3.3. Significance of the temporal variability

Figure 8 shows the spatial distribution of grid points at which the QPM anomalies of HRI, PDD, and MDS exhibited oscillation high (OH) or low (OL) periods significant at the 5% level. For the variation in the HRI and PDD, there were more grid points with significant OH and OL periods in the Central than the Southern and Northern regions (Figures 8(a), (b), (d) and (e)). The MDS exhibited more significant OLs than OHs (Figures 8(c) and (f)). Significant OHs of PDD and MDS indicate severe drought conditions. Due to prolonged and severe drought conditions, some areas within the study area experience famine or food insecurity due to failure of rain-fed crops, and death of animals. Drought conditions also affect the flow control for ecological purposes such as compensation flows and dilution flows for improving the water quality for power generating plants. Significant OHs of HRI lead to floods, landslides, and so forth, which are not exceptional to the study area as highlighted in Section 1.

4. Conclusions

This study assessed the spatio-temporal variability in extreme daily rainfall quantiles in the Nile basin. The variability analyses were based on the QPM applied to high resolution ($0.5^\circ \times 0.5^\circ$) gridded rainfall from the PGFs covering the period 1948–2010. Three metrics were

considered including: (1) the ten HRI in each year, (2) the PDD in each year, and (3) the MDS in each year. The co-variation of extreme rainfall and the large-scale ocean–atmosphere conditions was also investigated.

In the Northern part of the basin, which is characterized by arid conditions, the HRI were characterized by negative (positive) anomalies from the 1940s to early 1980s (mid-1980s to late 2000s). For the Central region, the HRI was above the long-term average (or reference) from the 1950s to early 1960s. From the mid-1960s to the 1980s, the HRI anomalies were below the reference. For the equatorial region in the Southern part of the Nile basin, oscillation highs were from the late 1950s to mid-1960s, and again in the late 1990s, while the oscillation lows were in the 1970s and the 1980s.

In the Northern region, the low rainfall intensities were below (above) the reference from the early 1980s to late 2000s (1950s and 1970s). For the Central region, the drought conditions from the late 1970s to early 2000s (1950s to mid-1960s) were above (below) the reference. For the equatorial region, the low rainfall intensities exhibited oscillation low (high) from the mid-1950s to early 1970s (1980s to 2000s).

This study shows that the variation in the metrics HRI, PDD, and MDS during 15-year periods is oscillatory in nature. Based on the latitudinal difference in the variation of these extreme rainfall metrics, the study area can be divided into three regions namely the Northern, Central, and equatorial (or Southern) regions. For the Central region, the variability in the extreme rainfall is dominantly driven by the variation in the sea surface temperatures of the Atlantic and Pacific Oceans. For the equatorial (or Southern) region, the extreme rainfall variability is primarily linked to the anomalies in the sea level pressure in the North Atlantic Ocean and the variation in the sea surface temperature of the Indian Ocean. The variability in the extreme rainfall of the Northern region corresponds to the anomalies in sea surface temperatures of the Indian and Atlantic Oceans as well as from the Pacific Ocean.

The findings from this study are important for various applications that are related to extreme rainfall conditions in the study area.

Acknowledgements

The gridded rainfall data used were based on the Princeton global forcings obtained online from http://hydrology.princeton.edu/data/pgf/ (accessed 12 February 2016). This research was financially supported by an IRO Ph.D. scholarship of KU Leuven. The authors declare no conflict of interest.

References

Abtew W, Melesse AM, Dessalegne T. 2009. El Niño southern oscillation link to the Blue Nile River basin hydrology. *Hydrol. Process.* **23**: 3653–3660.

Berhane F, Zaitchik B, Dezfuli A. 2014. Subseasonal analysis of precipitation variability in the Blue Nile River basin. *J. Clim.* **27**(1): 325–344.

Block P, Rajagopalan B. 2007. Interannual variability and ensemble forecast of Upper Blue Nile basin Kiremt season precipitation. *J. Hydrometeorol.* **8**(3): 327–343.

Diro GT, Grimes DIF, Black E. 2011. Teleconnections between Ethiopian summer rainfall and sea surface temperature: Part I. Observation and modelling. *Climate Dynam.* **37**(1): 103–119.

Ezekiel M. 1930. *Methods of Correlational Analysis*. John Wiley and Sons: New York, NY.

Fontaine B, Roucou P, Trzaska S. 2003. Atmospheric water cycle and moisture fluxes in the West African monsoon: mean annual cycles and relationship using NCEP/NCAR reanalysis. *Geophys. Res. Lett.* **30**(3): 3–6.

Hoell A, Shukla S, Barlow M, Cannon F, Kelley C, Funk C. 2015. The forcing of monthly precipitation variability over Southwest Asia during the Boreal Cold Season. *J. Clim.* **28**(18): 7038–7056.

Hulme M. 1992. Rainfall changes in Africa: 1931–1960 to 1961–1990. *Int. J. Climatol.* **12**: 685–699.

Jones PD, Jonsson T, Wheeler D. 1997. Extension to the North Atlantic oscillation using early instrumental pressure observations from Gibraltar and south-west Iceland. *Int. J. Climatol.* **17**(13): 1433–1450.

Jury MR. 2010. Ethiopian decadal climate variability. *Theor. Appl. Climatol.* **101**(1): 29–40.

Kalnay E, Kanamitsu M, Kistler R, Collins W, Deaven D, Gandin L, Iredell M, Saha S, White G, Woollen J, Zhu Y, Leetmaa A, Reynolds R, Chelliah M, Ebisuzaki W, Higgins W, Janowiak J, Mo KC, Ropelewski C, Wang J, Jenne R, Joseph D. 1996. The NCEP/NCAR 40-year reanalysis project. *Bull. Am. Meteorol. Soc.* **77**(3): 437–471.

Long M, Entekhabi D, Nicholson SE. 2000. Interannual variability in rainfall, water vapor flux, and vertical motion over West Africa. *J. Clim.* **13**(21): 3827–3841.

Nicholson SE. 1996. A review of climate dynamics and climate variability in Eastern Africa. In *The Limnology, Climatology and Paleoclimatology of the East African Lakes*, Johnson TC, Odada EO (eds). Gordon and Breach: Amsterdam, The Netherlands, 25–26.

Nicholson SE, Kim J. 1997. The relationship of the El Nino-Southern Oscillation to African rainfall. *Int. J. Climatol.* **17**: 117–135.

Nyeko-Ogiramoi P, Willems P, Ngirane-Katashaya G. 2013. Trend and variability in observed hydrometeorological extremes in the Lake Victoria basin. *J. Hydrol.* **489**: 56–73.

van Oldenborgh GJ, te Raa LA, Dijkstra HA, Philip SY. 2009. Frequency- or amplitude-dependent effects of the Atlantic meridional overturning on the tropical Pacific Ocean. *Ocean Sci.* **5**: 293–301.

Onyutha C. 2016a. Statistical analyses of potential evapotranspiration changes over the period 1930–2012 in the Nile River riparian countries. *Agric. For. Meteorol.* **226–227C**: 80–95.

Onyutha C. 2016b. Geo-spatial trends and decadal anomalies in extreme rainfall over Uganda, East Africa. *Adv. Meteorol.* **2016**: 1–15.

Onyutha C, Willems P. 2015. Spatial and temporal variability of rainfall in the Nile Basin. *Hydrol. Earth Syst. Sci.* **19**(5): 2227–2246.

Onyutha C, Willems P. 2017. Influence of spatial and temporal scales on statistical analyses of rainfall variability in the River Nile basin. *Dyn. Atmos. Oceans* **77**: 26–42.

Onyutha C, Tabari H, Rutkowska A, Nyeko-Ogiramoi P, Willems P. 2016. Comparison of different statistical downscaling methods for climate change rainfall projections over the Lake Victoria basin considering CMIP3 and CMIP5. *J. Hydro-Environ. Res.* **12**: 31–45.

Phillips J, McIntyre B. 2000. ENSO and interannual rainfall variability in Uganda: implications for agricultural management. *Int. J. Climatol.* **20**: 171–182.

Pradhan M, Yadav RK, Ramu Dandi A, Srivastava A, Phani MK, Rao SA. 2017. Shift in MONSOON – SST teleconnections in the tropical Indian Ocean and ENSEMBLES climate models' fidelity in its simulation. *Int. J. Climatol.* **37**: 2280–2294.

Rayner NA, Parker DE, Horton EB, Folland CK, Alexander LV, Rowell DP, Kent EC, Kaplan A. 2003. Global analyses of sea surface temperature, sea ice, and night marine air temperature since the late nineteenth century. *J. Geophys. Res.* **108**(D14): 4407.

Schreck CJ, Semazzi FHM. 2004. Variability of the recent climate of eastern Africa. *Int. J. Climatol.* **24**(6): 681–701.

Seleshi Y, Demaree GR. 1995. Rainfall variability in the Ethiopian and Eritrean Highlands and its links with the Southern Oscillation Index. *J. Biogeogr.* **22**(4/5): 945–952.

Seleshi Y, Zanke U. 2004. Recent changes in rainfall and rainy days in Ethiopia. *Int. J. Climatol.* **24**(8): 973–983.

Sheffield J, Goteti G, Wood EF. 2006. Development of a 50-year high-resolution global dataset of meteorological forcings for land surface modeling. *J. Clim.* **19**(13): 3088–3111.

Taye MT, Willems P. 2012. Temporal variability of hydroclimatic extremes in the Blue Nile basin. *Water Resour. Res.* **48**(3): 1–13.

Thiery W, Davin E, Panitz H-J, Demuzere M, Lhermitte S, Van Lipzig NPM. 2015. The impact of the African Great Lakes on the regional climate. *J. Clim.* **28**: 4061–4085.

Tierney JE, Smerdon JE, Anchukaitis KJ, Seager R. 2013. Multidecadal variability in East African hydroclimate controlled by the Indian Ocean. *Nature* **493**(7432): 389–392.

Trenberth KE. 1997. The definition of El Nino? *Bull. Am. Meteorol. Soc.* **78**(12): 2771–2777.

Willems P. 2013. Multidecadal oscillatory behaviour of rainfall extremes in Europe. *Clim. Change* **120**(4): 931–944.

Zeng R, Cai X. 2016. Climatic and terrestrial storage control on evapotranspiration temporal variability: Analysis of river basins around the world. *Geophys. Res. Lett.* **43**(1): 185–195.

Zhang Z, Xu C-Y, El-Tahir ME-H, Cao J, Singh VP. 2012. Spatial and temporal variation of precipitation in Sudan and their possible causes during 1948–2005. *Stoch. Environ. Res. Risk Assess.* **26**(3): 429–441.

Zilli M, Carvalho LMV, Liebmann B, Silva Dias MA. 2017. A comprehensive analysis of trends in extreme precipitation over Southeastern coast of Brazil. *Int. J. Climatol.* **37**: 2269–2279.

